**Eurasian Journal of Physics and Functional Materials**

**2026, 10(4), 399-424**

# Detector-Level Transport Regimes in Polyethylene/Aluminium Shielding of Silicon Sensors under Photon, Electron, and Proton Irradiation

Y. Havvat

Department of Physics, Cukurova University, Adana, Turkey

E-mail: havvatyusuf249@gmail.com

DOI: **10.32523/ejpfm.2026100405**
Received: 29 September 2026
Revised: 10 November 2026
Accepted: 16 November 2026

Shielding performance inferred from attenuation or nominal thickness can misrepresent the response of a finite semiconductor detector. This study uses Geant4 to map energy deposited in a silicon sensor of dimensions $20\ \text{mm} \times 20\ \text{mm} \times 0.5\ \text{mm}$ behind polyethylene (PE) and PE–aluminium (PE–Al) shields under controlled photon, electron, and proton fields. Event-level scoring separates primary survival, residual entry energy, shield-generated secondaries, and finite shield coverage. The proton response was strongly non-monotonic near range-out: effective suppression occurred between 8–9 mm PE at 30 MeV and between 20–25 mm PE at 50 MeV, in agreement with NIST PSTAR projected ranges. For photons, short shield-to-sensor gaps increased silicon energy deposition, consistent with enhanced acceptance of shield-generated secondaries. At the final 100 mm gap, adding 0.5 mm Al to 25 mm PE improved the photon-response reduction by $3.083 \pm 0.558$ percentage points under the reference physics list; the uncertainty is a two-sided 95% sampling confidence-interval half-width and excludes physics-model uncertainty. An XCOM narrow-beam calculation gave 1.01 percentage points of additional uncollided primary-photon number removal, a different observable that cannot be subtracted from the detector-response change to quantify a secondary contribution. A finite-size test further showed that oblique protons could traverse an edge-clipped path in a nominally thick shield. Within the discrete candidate set, 25 mm PE was the lowest-mass configuration with positive mean response reduction in all four benchmark fields. These results define transport and geometry regimes that should be checked before a shielding design is advanced to mission-specific modelling or experimental qualification.

**Keywords:** Geant4; silicon detector; polyethylene; aluminium; radiation shielding; secondary particles; proton range-out.

# 1. Introduction

Silicon sensors and associated electronics may be exposed to photons, electrons, protons, and secondary particles generated in nearby materials. Depending on particle type and energy, these fields can produce ionising dose, displacement damage, transient response changes, and single-event effects [1–3]. Shielding is therefore central to the design of semiconductor instrumentation for space, aerospace, accelerator, and other radiation-prone environments.

Operational fields commonly contain broad energy and angular distributions and more than one particle species [4]. As a result, shield performance is not a function of thickness alone. Composition, areal density, layer order, secondary production, and the relative dimensions of the source, shield, and detector all affect the energy ultimately deposited in a sensitive volume. Multilayer and graded structures, low- and high- $Z$ combinations, and mass-aware optimisation have consequently received sustained attention [5–9]. A persistent interpretive problem, however, is that attenuation within a shield is not equivalent to response reduction in a downstream detector.

For protons, a sub-range layer may slow rather than stop the primary population. The transmitted protons can then enter silicon at an energy where their stopping power is higher, so the shield increases detector energy deposition before a slightly thicker layer produces range-out. NIST PSTAR data provide an independent reference for this critical thickness [10–12]. Electron transport couples collisional losses to multiple scattering and radiative production; both range and finite detector acceptance therefore matter, with ESTAR data providing a corresponding range reference [13, 14].

Photon shielding poses a different detector-level problem. Interactions in the shield generate electrons and positrons that can carry energy toward the sensor. Their contribution depends on direction and geometric acceptance, so changing the shield-to-sensor gap can alter silicon energy deposition without changing the material attenuation coefficient. XCOM data can quantify the expected removal of uncollided primary photons, but not the complete finite-geometry detector response [15]. Likewise, an oblique charged particle may enter through a side surface and traverse less material than a front-to-back path would imply. Finite edge coverage must therefore be distinguished from complete shield bypass.

Geant4 provides electromagnetic and hadronic transport, secondary generation, and energy-deposition scoring in user-defined geometries [16–18]. Here, Geant4 and ROOT [19] are used to place proton range-out, photon-secondary transport, and finite lateral containment in a single detector-response framework. The benchmark fields are deliberately controlled rather than mission-specific: photons and electrons follow a discrete particle-number distribution from 0.1–10 MeV, and protons are simulated at 30 MeV and 50 MeV.

The contribution is a transport-regime map linking mean silicon energy deposition to primary entry, residual entry energy, secondary origin, shield-to-sensor spacing, and edge-clipped transport. It addresses four design questions: when partial proton slowing becomes harmful; when shield-generated secondaries reverse the expected photon benefit; when finite coverage invalidates a one-

dimensional stopping argument; and which members of the tested PE/Al set retain positive response reduction across all benchmark fields at the lowest active mass. PSTAR, ESTAR, and XCOM comparisons, repeated seeds, production-cut refinement, and an alternative electromagnetic configuration are used to delimit–rather than overstate–the predictive scope of the Monte Carlo results.

# 2. Simulation and analysis framework

## 2.1 Geant4 model and benchmark geometry

Particle transport used Geant4 11.2.0 [16–18]. The Shielding reference physics list was selected [20, 21]. ROOT 6.34.04 was used for event-level data analysis [19]. The study developed through separate simulation and analysis campaigns. The retained application and campaign-specific shell scripts specify runtime controls for particle type and energy, incidence angle, shield composition, thickness, layer order, shield-to-sensor spacing, and lateral dimensions. Campaign settings are distinguished below rather than treated as one unchanged simulation configuration.

The sensitive detector was represented by a homogeneous $20\ \text{mm} \times 20\ \text{mm} \times 0.5\ \text{mm}$ silicon volume ($\rho = 2.329\ \text{g/cm}^3$) inside an air-filled world. The shielding consisted of polyethylene (PE, $\rho = 0.94\ \text{g/cm}^3$), optionally followed by a downstream aluminium layer (Al, $\rho = 2.699\ \text{g/cm}^3$), with the ordering

$$\text{source} \rightarrow \text{PE} \rightarrow \text{Al} \rightarrow \text{Si}.$$

The final benchmark geometry used $200\ \text{mm} \times 200\ \text{mm}$ shield layers, a 100 mm distance between the rear shield surface and the silicon sensor, and a 210 mm source-to-sensor-centre distance. Smaller gaps and lateral dimensions were used only in the dedicated secondary-transport and finite-containment studies.

The discrete design comparison used PE thicknesses of 9 mm, 15 mm, 20 mm, and 25 mm. Two additional candidates consisted of 25 mm PE backed by either 0.5 mm or 1.0 mm Al. Separate mechanism scans used 6–9 mm PE for 30 MeV protons, 20 mm and 25 mm PE for 50 MeV protons, shield-to-sensor gaps of 5 mm, 20 mm, 50 mm, and 100 mm, and the angle/coverage combinations discussed in Section 4.3. These diagnostic scans explain the response regimes; they are not additional members of the final mass–performance comparison.

Region-dependent production cuts of $1\ \mu\text{m}$ in silicon and $10\ \mu\text{m}$ in the shielding volumes were used. The event-level scoring retained total silicon energy deposition, particle identity, parent and creator information, production volume, sensor entry, entry kinetic energy, and dedicated primary-proton transport checkpoints at PE entry, forward PE exit, and silicon entry. Figure 1 shows the layer order, scoring checkpoints, and dimensions used in the final benchmark geometry.

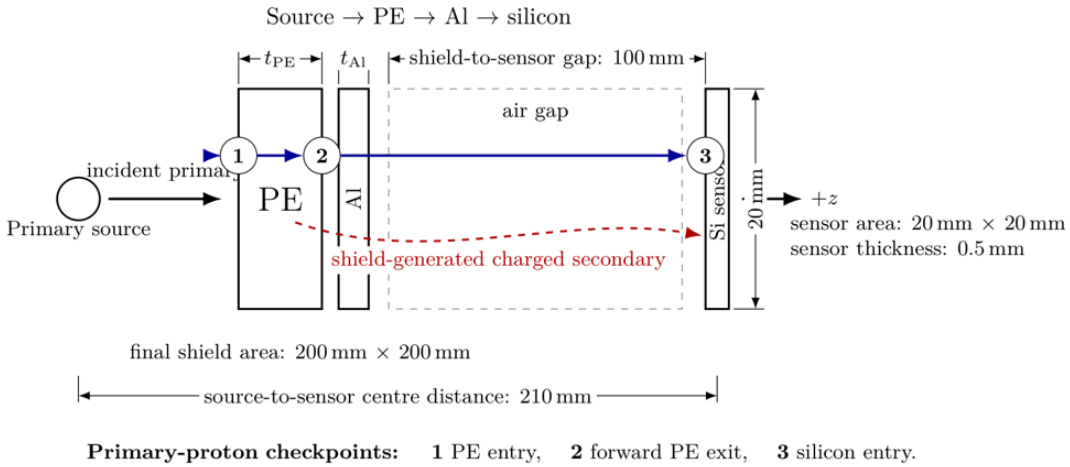


Figure 1. Benchmark geometry and transport checkpoints. The final configuration used a 200 mm × 200 mm PE shield, optional downstream Al, a 100 mm shield-to-sensor gap, and a 20 mm × 20 mm × 0.5 mm silicon sensor. Markers 1–3 denote primary-proton entry into PE, forward PE exit, and silicon entry, respectively; the dashed trajectory illustrates a shield-generated charged secondary. The schematic is not to scale.

## 2.2 Benchmark irradiation fields

Photon and electron primaries were sampled from the common discrete particle-number distribution listed in Table 1. The distribution was selected to provide controlled energy-dependent transport comparisons and was not intended to represent a specific operational radiation environment.

Table 1.
Discrete benchmark photon and electron energy distribution.

| $E$ (MeV) | 0.1 | 0.2 | 0.3 | 0.4 | 0.5 | 1 | 2 | 5 | 10 |
|---|---|---|---|---|---|---|---|---|---|
| $p$ | 0.20 | 0.18 | 0.15 | 0.12 | 0.10 | 0.10 | 0.07 | 0.05 | 0.03 |

Proton calculations used monoenergetic 30 MeV and 50 MeV primaries to resolve the transition between incomplete slowing and effective range-out in PE. The principal calculations used normal incidence, while dedicated oblique-incidence simulations were used to examine finite lateral containment.

The source was configured as either a pencil beam or a uniform square distribution according to the individual simulation campaign. Results obtained with different source modes, gaps, shield dimensions, or event counts were not pooled as estimates of the same configuration. Every protection value was formed with an unshielded reference that used the same field definition, source mode, detector geometry, and event normalisation as its shielded counterpart.

Table 2 consolidates the settings from the retained source, campaign scripts, analysis macros, and processed results. The diagnostic campaigns use a pencil beam, whereas the final candidate and validation campaigns explicitly select a uniform square source of side length 20 mm. Source size denotes the launch-plane distribution, not the shield area or an isotropic angular distribution.

Table 2.
Campaign-specific source and geometry settings. $W$ is the square shield side length and $g$ is the distance along $z$ from the rear shield surface to the front silicon surface. Dimensions are in mm. The source centre is 210 mm upstream of the sensor centre along the beam axis in every listed campaign.

| Comparison | Field / PE thickness | Source mode and size | $W$; $g$ | Incidence angle | Independent runs and primaries per run |
|---|---|---|---|---|---|
| Photon gap scan (27) | $\gamma$; 25, with/without 0.5 Al | Pencil; point launch | 100; 5, 20, 50, 100 | 0° | $3 \times 10^5$ per configuration |
| Species/origin diagnostic (25) | $\gamma$; no shield, 25, 25 + 0.5 Al | Pencil; point launch | 100; 20 | 0° | $3 \times 10^5$ per configuration |
| Exploratory thickness (19–20) | Protons; 30, 50 MeV | Pencil; point launch | 100; 20 | 0° | $3 \times 5 \times 10^4$ per configuration |
| Proton transport (26) | 30 MeV: 0, 8, 9; 50 MeV: 0, 20, 25 | Pencil; point launch | 100; 20 | 0° | $3 \times 10^5$ per configuration |
| Proton angle scan (27) | 30 MeV / 9; 50 MeV / 25 | Pencil; point launch | 100; 20 | 0°, 30°, 45°, 60° | $3 \times 3 \times 10^4$ per angle/configuration |
| Side-length scan (27A) | 30 MeV / 9; 50 MeV / 25 | Pencil; point launch | 100, 200, 300; 20 | 60° | $3 \times 10^5$ per size/configuration |
| Candidate comparison (28–30A) | All four fields; six designs | Uniform square; $20 \times 20$ | 200; 100 | 0° | $3 \times 5 \times 10^5$ photons; $3 \times 10^5$ electrons/protons |
| Final validation (28–29) | All four fields; two selected designs | Uniform square; $20 \times 20$ | 200; 100 | 0° | $5 \times 5 \times 10^5$ photons; $5 \times 10^5$ electrons/protons |
| Cut / model checks | $\gamma$; selected designs | Uniform square; $20 \times 20$ | 200; 100 | 0° | Cuts: $3 \times 5 \times 10^5$; alternative model: $1 \times 5 \times 10^5$ |

*Note:* Numbers in parentheses identify the archived simulation steps. Products denote independent runs multiplied by primaries per run, using the event counts specified in the campaign scripts. The proton-transport and side-length analysis macros also use $10^5$ histories per seed as their explicit normalisation. The equal-statistics photon rerun (30A) replaces the earlier $3 \times 10^5$-photon-per-seed candidate scan; it is not pooled with it. Pencil mode has zero transverse launch extent.

**Implemented oblique geometry**

The shield and silicon remain parallel to the $xy$ plane, without volume rotation. The beam is rotated in the $xz$ plane (azimuth $0^\circ$), with direction

$$\mathbf{d} = (\sin\theta, 0, \cos\theta).$$

For the sensor centre $\mathbf{r}_{\mathrm{Si}} = (0, 0, 10)$ mm and $L = 210$ mm, the launch point is

$$\mathbf{r}_0 = \mathbf{r}_{\mathrm{Si}} - L\mathbf{d} + u\mathbf{e}_u + v\mathbf{e}_v, \tag{1}$$

where

$$\mathbf{e}_u = (\cos\theta, 0, -\sin\theta)$$

and

$$\mathbf{e}_v = (0, 1, 0).$$

Pencil campaigns set $u = v = 0$; square-source campaigns sample $u, v$ independently and uniformly in $[-10, 10]$ mm. All primaries are parallel to $\mathbf{d}$; the central ray is aimed at the silicon centre. At normal incidence the source plane is $z = -200$ mm. The gap is measured along $z$, not along an oblique ray; a central straight ray crosses an axial gap $g$ over distance $g/\cos\theta$.

## 2.3 Detector response and statistical treatment

For each event, the detector response was defined as the total energy deposited by all particle steps in the silicon sensitive volume,

$$E_{\mathrm{dep}} = \sum_{k \in \mathrm{Si}} \Delta E_k, \tag{2}$$

For comparisons between shielded and unshielded configurations, the principal response metric was

$$P = 100 \left( 1 - \frac{\overline{E}_{\mathrm{dep,shielded}}}{\overline{E}_{\mathrm{dep,ref}}} \right), \tag{3}$$

where $\overline{E}_{\mathrm{dep}}$ is the mean silicon energy deposition per generated primary. Positive $P$ denotes a reduction in detector response, whereas negative $P$ indicates that the shield increased the response relative to the unshielded reference.

Particle species, parent and creator information, secondary-production volume, primary-particle sensor entry, kinetic energy at sensor entry, and the proton checkpoints in Fig. 1 were used to identify the physical origin of the observed detector response. The checkpoint record distinguishes a primary that intersects PE from one that bypasses it entirely. Intersection alone does not establish full front-to-back traversal or identify a lateral exit face.

Repeated calculations used independent Geant4 random-number seed pairs. Ensemble uncertainties are reported as two-sided 95% confidence intervals based on the Student-$t$ distribution. Protection was evaluated for corresponding seed indices before averaging across the ensemble. Matching the initial seed settings provided a consistent campaign structure but does not imply identical event-by-event random-number histories after particle trajectories diverge.

The equal-statistics photon candidate comparison used three independent runs of $5 \times 10^5$ primaries for each configuration. Final validation of the two selected designs used five independent seed pairs, with $5 \times 10^5$ photons per seed and $1 \times 10^5$ particles per seed for the electron, 30 MeV proton, and 50 MeV proton fields.

When no sensor-entry or sensor-deposition event was observed, the result was reported as below the practical statistical resolution of the simulation campaign rather than as exact zero response or exact 100% protection.

**Sampling intervals and physics-model dependence**

For the final photon contrast, let

$$d_i = P_{\gamma,\mathrm{PE+Al},i} - P_{\gamma,\mathrm{PE},i}$$

be the difference for seed index $i$. The reported interval is

$$\overline{d} \pm t_{0.975,n-1}\frac{s_d}{\sqrt{n}}, \qquad n = 5, \tag{4}$$

where $s_d$ is the sample standard deviation of the five run-level differences. Thus $3.083 \pm 0.558$ percentage points corresponds to $[2.525, 3.641]$ percentage points for Monte Carlo sampling variability at fixed source, geometry, cuts, and reference physics list. It is not an interval that includes uncertainty in electromagnetic interaction models or cross sections.

**Upper confidence bound for zero primary-proton entries**

Let $K$ count generated-primary histories in which the original primary proton enters silicon at least once, with $N$ independently simulated, unweighted histories of the same configuration. Each history is counted once, irrespective of repeated boundary crossings. Under a binomial model,

$$\Pr(K = 0 \mid p_{\mathrm{entry}}) = (1 - p_{\mathrm{entry}})^N.$$

Inverting this probability gives the exact one-sided 95% upper bound [22]

$$p_{\mathrm{entry},u} = 1 - 0.05^{1/N} \approx \frac{-\ln(0.05)}{N} = \frac{2.996}{N}, \qquad K = 0. \tag{5}$$

Table 6 applies this bound to the diagnostic conditions with zero reported original-primary entries. Each limit uses only the three seeds of one fixed condition and the documented event count, not a sum over different energies, angles, or shield sizes. The final-validation energy-response summaries alone do not establish zero primary entries and are not assigned a zero-count limit.

Equation 5 bounds a primary-entry probability. It does not bound the energy-weighted response in Eq. 3. A nonzero deposition can remain when the original primary proton never enters silicon, for example through transported secondaries. Conversely, a very small energy-deposition ratio does not establish $K = 0$. The reported $P > 99.9999\%$ values therefore describe the finite-run energy-deposition estimates, not a 95% lower confidence bound on proton rejection or on energy-response reduction.

### 2.4 Multi-field and mass metrics

The active shielding mass was calculated from the density, area, and thickness of each layer,

$$m = \sum_i \rho_i A_i t_i, \tag{6}$$

and excludes supports, adhesives, fasteners, and other integration hardware.

Each candidate was evaluated under the four benchmark fields through

$$\mathbf{P} = \left(P_\gamma, P_e, P_{p30}, P_{p50}\right), \tag{7}$$

and the limiting multi-field response was defined as

$$P_{\text{worst}} = \min\left(P_\gamma, P_e, P_{p30}, P_{p50}\right). \tag{8}$$

Candidate configurations were compared using active shield mass and $P_{\text{worst}}$. This criterion prevents favourable performance in one radiation field from concealing an adverse response in another and is used here as a comparative screening metric rather than as a claim of global optimisation.

## 3. Verification and sensitivity analysis

### 3.1 Repeated-seed stability

Five independent seed-index-matched runs were used for the final comparison between 25 mm PE and 25 mm PE plus 0.5 mm Al. Stability was assessed from the distribution of run-level response reductions and, for the photon comparison, from the within-index difference between the two configurations. All five photon differences favoured the aluminium-backed shield. The complete estimates and confidence intervals are reported once, with the final multi-field results, in Section 4.4.

### 3.2 Production-cut sensitivity

A production-cut sensitivity check was performed for the final photon configurations using three matched random-seed pairs and $5 \times 10^5$ primary photons per seed. The reference production cuts of 1 $\mu$m in silicon and 10 $\mu$m in the shielding regions were refined to 0.1 $\mu$m and 1 $\mu$m, respectively, while the source, geometry, event count, and initial random-seed settings were kept unchanged.

For 25 mm PE, the mean photon-response reduction changed from 16.969% to 15.386%, corresponding to a matched difference of $-1.583$ percentage points. For 25 mm PE + 0.5 mm Al, the corresponding values changed from 17.111% to 19.015%, giving a matched difference of 1.903 percentage points.

The two-sided 95% confidence intervals of both matched differences included zero. Thus, the three-seed comparison did not resolve a statistically significant systematic shift under the tested production-cut refinement, although a smaller transport-threshold dependence cannot be excluded. The reference production cuts were therefore retained for the final simulation campaigns.

## 3.3 Electromagnetic-model sensitivity

Electromagnetic-model sensitivity was examined by repeating the final photon configurations with the `Shielding_EMZ` reference physics list while retaining the same source, geometry, production-cut, event-count, and initial random-seed settings.

For 25 mm PE, the photon-response reduction changed from 15.322% with Shielding to 9.071% with `Shielding_EMZ`, a difference of $-6.251$ percentage points. In contrast, for 25 mm PE + 0.5 mm Al, the corresponding values were 18.331% and 18.445%, differing by only 0.114 percentage point.

The associated aluminium-backed minus PE-only contrasts were 3.009 percentage points for Shielding and 9.374 percentage points for `Shielding_EMZ`, a difference of 6.365 percentage points between these single-seed estimates. This change is much larger than the 0.558 percentage-point sampling half-width from the separate five-seed reference-list campaign. The two campaigns have different statistical roles: the five-seed interval quantifies sampling variability conditional on Shielding, while the single-seed comparison indicates that the improvement magnitude can depend on the transport configuration. Because sampling noise is also present in the single-seed estimates, neither 6.365 percentage points nor an envelope of the two contrasts is adopted as a physics-model uncertainty. Repeated seeds for each alternative list would be needed to quantify that dependence. In particular, the small shift in the PE–Al point estimate alone does not establish its model invariance.

## 3.4 PSTAR consistency of the proton transition regions

The proton critical-thickness regions obtained in Geant4 were compared with stopping-power and range data from the NIST PSTAR database [10–12]. Because the present calculations used normally incident protons and planar PE layers, the PSTAR projected range provides the most direct reference for the simulated stopping transition. The PSTAR polyethylene density, 0.94 $g/cm^3$, is identical to that used in the Geant4 model.

Table 3 compares the PSTAR projected ranges with the critical PE thickness intervals identified in Geant4.

Table 3.
Comparison of the Geant4 proton critical-thickness regions with NIST PSTAR projected ranges in polyethylene.

| $E_p$ | $R_{\mathrm{proj}}$ | $R_{\mathrm{proj}}$ | Geant4 transition |
|---|---|---|---|
| (MeV) | ($g/cm^2$) | (mm) | (mm) |
| 30 | 0.8233 | 8.76 | 8–9 |
| 50 | 2.079 | 22.12 | 20–25 |

For 30 MeV protons, the PSTAR projected range of 8.76 mm lies directly within the 8–9 mm Geant4 transition region. The areal densities of the 8 mm and 9 mm PE layers are 0.752 $g/cm^2$ and 0.846 $g/cm^2$, respectively, thereby bracketing the

PSTAR projected range of 0.8233 $g/cm^2$. This is consistent with the observed collapse of the primary-proton sensor-entry fraction between 8 mm and 9 mm.

The same correspondence was observed at 50 MeV. The PSTAR projected range of 22.12 mm (2.079 $g/cm^2$) lies between the tested 20 mm and 25 mm PE layers, whose areal densities are 1.880 $g/cm^2$ and 2.350 $g/cm^2$, respectively. At 20 mm, approximately 92.62% of the primary protons still entered the silicon with a mean entry energy of approximately 13.31 MeV, whereas no primary-proton sensor entry was observed in the corresponding 25 mm sample.

The agreement can therefore be summarised as

$$\sigma_8 < R_{\mathrm{proj},30} < \sigma_9, \tag{9}$$

$$\sigma_{20} < R_{\mathrm{proj},50} < \sigma_{25}. \tag{10}$$

Thus, the PSTAR projected ranges fall within both Geant4 critical-thickness intervals, supporting the interpretation that the non-monotonic detector response originates from the transition between incomplete proton slowing and effective range-out in polyethylene. Exact numerical agreement is not expected because Geant4 additionally accounts for stochastic energy loss, multiple scattering, nuclear interactions, secondary-particle production, and the finite simulation geometry.

## 3.5 ESTAR consistency of the electron response

The electron-shielding results were compared with stopping-power and range data from the NIST ESTAR database [10, 13, 14]. The final 25 mm PE layer corresponds to an areal density of 2.35 $g/cm^2$. Representative ESTAR CSDA ranges in polyethylene are approximately $4.22 \times 10^{-2}$ $g/cm^2$ (0.45 mm) at 0.2 MeV and $4.16 \times 10^{-1}$ $g/cm^2$ (4.42 mm) at 1 MeV. Thus, the PE layer substantially exceeds the reference CSDA ranges over the low-energy region containing 85% of the primary-electron probability in the benchmark distribution.

This range comparison is consistent with the approximately 99% reduction of the broadband electron response obtained in Geant4. For the remaining higher-energy component, the detector response also depends on multiple scattering, secondary-particle production, finite detector acceptance, and the 100 mm shield-to-sensor gap. The ESTAR comparison should therefore be regarded as an independent physical-consistency check rather than as a validation of the complete Geant4 electron transport model.

## 3.6 XCOM consistency of the photon response

The photon calculations were compared with independent attenuation data from the NIST XCOM database and the associated NIST photon mass-attenuation tables [15]. The reference data provide the mass attenuation coefficient, $\mu/\rho$, and the mass energy-absorption coefficient, $\mu_{\mathrm{en}}/\rho$, for polyethylene and aluminium over the complete energy range of the benchmark photon distribution.

For a homogeneous layer of areal density $\sigma_m = \rho t$, the ideal uncollided narrow-beam transmission is

$$T(E) = \exp\left[-\left(\frac{\mu}{\rho}\right)_E \sigma_m\right]. \tag{11}$$

For the final shielding configurations, the areal densities were 2.35 g/cm$^2$ for 25 mm PE and 0.13495 g/cm$^2$ for the 0.5 mm Al backing. The corresponding multilayer transmission was evaluated as

$$T_{\mathrm{PE+Al}}(E) = \exp\left[-\left(\frac{\mu}{\rho}\right)_{\mathrm{PE},E} \sigma_{\mathrm{PE}} - \left(\frac{\mu}{\rho}\right)_{\mathrm{Al},E} \sigma_{\mathrm{Al}}\right]. \tag{12}$$

Table 4 lists the NIST coefficients at the nine benchmark photon energies together with the calculated uncollided transmissions through the final PE and PE–Al configurations.

Table 4.
NIST photon mass attenuation and mass energy-absorption coefficients for polyethylene and aluminium at the benchmark energies, together with ideal narrow-beam transmission estimates for 25 mm PE and 25 mm PE + 0.5 mm Al. The transmission estimates neglect scattered-photon buildup and charged-secondary transport.

| $E_\gamma$ | Polyethylene | | Aluminium | | $T_{\mathrm{PE}}$ | $T_{\mathrm{Al}}$ | $T_{\mathrm{PE+Al}}$ |
|---|---|---|---|---|---|---|---|
| (MeV) | $\mu/\rho$ | $\mu_{\mathrm{en}}/\rho$ | $\mu/\rho$ | $\mu_{\mathrm{en}}/\rho$ | | | |
| | (cm$^2$/g) | | (cm$^2$/g) | | | | |
| 0.1 | 0.1719 | 0.02423 | 0.1704 | 0.03794 | 0.6677 | 0.9773 | 0.6525 |
| 0.2 | 0.1402 | 0.03029 | 0.1223 | 0.02745 | 0.7193 | 0.9836 | 0.7075 |
| 0.3 | 0.1217 | 0.03276 | 0.1042 | 0.02816 | 0.7513 | 0.9860 | 0.7408 |
| 0.4 | 0.1089 | 0.03368 | 0.09276 | 0.02862 | 0.7742 | 0.9876 | 0.7646 |
| 0.5 | 0.09947 | 0.03390 | 0.08445 | 0.02868 | 0.7916 | 0.9887 | 0.7826 |
| 1.0 | 0.07262 | 0.03190 | 0.06146 | 0.02686 | 0.8431 | 0.9917 | 0.8361 |
| 2.0 | 0.05064 | 0.02677 | 0.04324 | 0.02266 | 0.8878 | 0.9942 | 0.8826 |
| 5.0 | 0.03045 | 0.01921 | 0.02836 | 0.01795 | 0.9309 | 0.9962 | 0.9274 |
| 10.0 | 0.02145 | 0.01506 | 0.02318 | 0.01650 | 0.9508 | 0.9969 | 0.9479 |

The XCOM coefficients show the expected reduction in attenuation efficiency with increasing photon energy. For example, the calculated PE transmission increases from 0.6677 at 0.1 MeV to 0.9508 at 10 MeV. This trend is consistent with the moderate broadband photon-response reduction obtained in Geant4, because the higher-energy component remains comparatively penetrating.

The thin aluminium backing introduces only a modest additional attenuation of the primary photon beam. Its calculated standalone transmission varies from 0.9773 at 0.1 MeV to 0.9969 at 10 MeV, indicating that its direct primary-photon removal alone cannot account for a large change in the downstream silicon response.

For the discrete benchmark spectrum, the particle-number-weighted uncollided transmission was calculated as

$$\overline{T} = \sum_{j=1}^{9} p_j \, T(E_j). \tag{13}$$

The resulting values were $\overline{T}_{\mathrm{PE}} = 0.7693$ and $\overline{T}_{\mathrm{PE+Al}} = 0.7592$, corresponding to ideal primary-photon removal fractions of 23.07% and 24.08%, respectively. Thus, the attenuation-only estimate predicts an additional primary-photon removal of

$$\Delta A_{\mathrm{primary}} = 1.01 \text{ percentage points} \tag{14}$$

when the 0.5 mm aluminium backing is added.

In contrast, the five-seed Geant4 detector-level comparison gave

$$\Delta P_\gamma = 3.083 \pm 0.558 \text{ percentage points}, \tag{15}$$

under the reference physics list, with a sampling interval defined in Eq. 4. The two numerical changes refer to different observables: XCOM describes removal of photons by number from an ideal uncollided beam, whereas the Geant4 metric is normalised to the total energy deposited in the downstream silicon volume. The Monte Carlo response therefore includes transmitted and scattered photons, electrons and positrons generated in the shielding, their residual energies and directions, and their probability of reaching the finite silicon sensor after the 100 mm air gap.

For example, the expected broadband detector response has the form

$$P_\gamma = 100 \left( 1 - \frac{\sum_j p_j \, \overline{E}_{\mathrm{dep,shield},E_j}}{\sum_j p_j \, \overline{E}_{\mathrm{dep,ref},E_j}} \right), \tag{16}$$

whose energy-dependent response weights differ from the number weights in Eq. 13. Consequently, $\Delta P_\gamma - \Delta A_{\mathrm{primary}}$ is not a measured secondary-particle contribution, and the fact that 3.083 exceeds 1.01 percentage points does not by itself establish a particular secondary mechanism. Such an attribution requires deposition and provenance tallies in the actual detector geometry.

The mass energy-absorption coefficients provide material-level context. At 0.1 MeV, $\mu_{\mathrm{en}}/\rho$ is larger for aluminium than for polyethylene, whereas across much of the intermediate benchmark range the two materials have comparable values. The effect of the aluminium backing therefore cannot be interpreted simply as increased bulk photon attenuation. Its detector-level contribution depends on the production and transport of charged secondaries, the downstream layer ordering, and the shield-to-sensor separation.

The XCOM comparison quantifies the decreasing uncollided attenuation efficiency with photon energy and the modest direct primary-photon number removal from the thin Al layer. It does not validate a numerical secondary contribution or predict the full silicon response. The comparison is an independent attenuation-consistency check rather than a complete validation of

the Geant4 photon model, since the ideal attenuation calculation does not include scattered-photon buildup, finite geometry, charged-secondary transport, or detector-response effects.

Taken together, the repeated-seed, production-cut, electromagnetic-model, PSTAR, ESTAR, and XCOM comparisons provide complementary tests of numerical stability and consistency with established stopping and attenuation physics. These checks do not constitute experimental validation or an independent transport-code benchmark; the results are therefore interpreted as a mechanism-resolved Geant4 benchmark assessment within the defined radiation fields and geometry.

# 4. Results and Discussion

## 4.1 Photon response and shield-to-sensor spacing

The broadband photon response depended strongly on the separation between the downstream shield surface and the silicon sensor. Figure 2 shows the response obtained with 25 mm PE and 25 mm PE + 0.5 mm Al for shield-to-sensor gaps between 5 mm and 100 mm.

At 5 mm, both configurations increased the silicon energy deposition relative to the unshielded reference, giving $P_\gamma = -96.78 \pm 21.87\%$ for PE and $-91.47 \pm 3.72\%$ for PE–Al. The adverse response decreased with increasing separation: at 20 mm, the corresponding values were $-44.72 \pm 11.08\%$ and $-35.27 \pm 8.25\%$. At 50 mm, the central estimates became positive ($1.91 \pm 14.92\%$ and $5.81 \pm 11.05\%$, respectively), although the confidence intervals still included zero. At the final 100 mm spacing, the exploratory gap campaign yielded $13.17 \pm 13.44\%$ for PE and $17.05 \pm 9.78\%$ for PE–Al. These three-seed values are distinct from the higher-statistics, five-seed final estimates in Table 7. They also use a pencil source and a 100-mm shield side, rather than the final square source and 200-mm shield side. Their overlapping intervals do not make them interchangeable estimates of one configuration.

The fraction of events with nonzero silicon energy deposition also decreased with increasing gap, from approximately 1.40% to 0.93% for PE and from 1.33% to 0.90% for PE–Al between 5 mm and 100 mm. The simultaneous reduction in the positive-event fraction and recovery of positive protection are consistent with a gap-dependent acceptance of transported secondaries and scattered photons. The observed gap dependence cannot be represented by a material attenuation coefficient alone. At short separations, charged secondaries generated in the shielding can reach the silicon more efficiently. The separate 20-mm-gap diagnostic below quantifies the deposited-energy partition at that setting, not its variation over the entire gap scan.

### Particle species and origin of deposited energy

The existing step-25 diagnostic records silicon energy deposition by depositing-particle species and immediate birth volume. With $s(k)$ denoting the species of

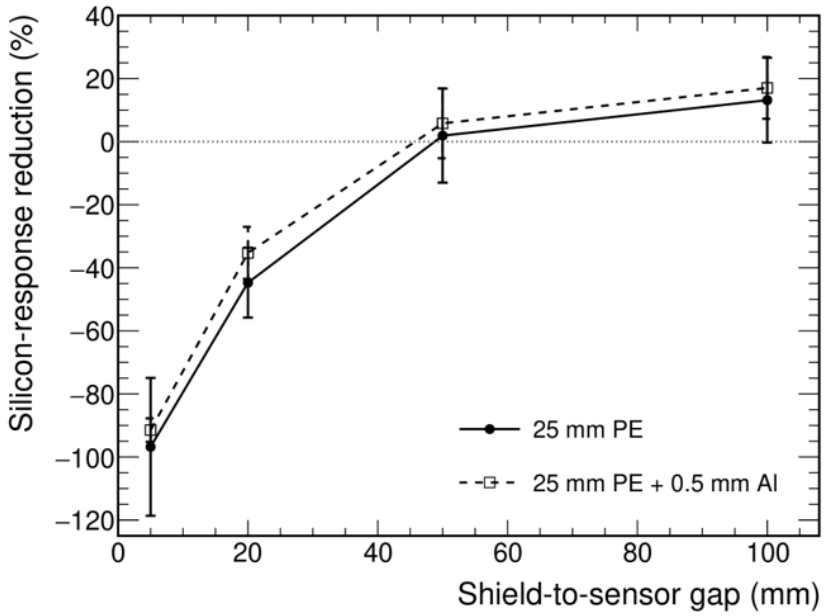


Figure 2. Broadband photon silicon-response reduction as a function of shield-to-sensor gap for 25 mm PE and 25 mm PE + 0.5 mm Al. Negative values indicate greater silicon energy deposition than in the matched unshielded reference. Error bars represent two-sided 95% confidence intervals from the three-seed pencil-beam campaign with 100-mm shield sides and $10^5$ photons per seed.

the depositing track, the partition is

$$\overline{E}_{\mathrm{dep}}^{(s)} = \frac{1}{N}\sum_{i=1}^{N}\sum_{\substack{k\in\mathrm{Si}\\ s(k)=s}} \Delta E_{ik}, \qquad \sum_{s}\overline{E}_{\mathrm{dep}}^{(s)} = \overline{E}_{\mathrm{dep}}. \tag{17}$$

The retained analysis first averages the per-primary energy tallies over the three seeds and then divides each component by the corresponding mean total. Table 5 gives these energy shares for the pencil beam, 100-mm shield side, 20-mm gap, and normal incidence. The unshielded case uses the same source and sensor.

Secondary electrons account for 97.97–99.20% of deposited energy, but this does not mean that all of their energy arrived from the shield: electrons born inside silicon are included. The origin tallies show that tracks born in PE contribute 30.34% of total deposition in the PE-only case; PE- and Al-born tracks together contribute 28.99% in the backed case. Silicon-born tracks contribute 68.73% and 70.34%, respectively. Thus the short-gap energy response contains a directly recorded shield-born secondary-track contribution alongside local conversion of photon energy in silicon.

The ten original species tallies close to the total to within $4.1 \times 10^{-5}$ percentage points at the precision of the retained CSV. Birth-volume shares classify the depositing track's own creation volume, not its full ancestry, and exclude primary-track deposition; they must not be added to the species shares as another component. Local deposition on a photon step follows the Geant4 scoring and production-cut convention and differs from photon energy entering silicon. This diagnostic supports the short-gap interpretation but does not supply species fractions for the different final 100-mm-gap geometry or isolate the origin of its 3.083-percentage-point contrast.

Table 5.
Existing photon deposited-energy diagnostic at a 20-mm gap (step 25; three seeds of $10^5$ photons). PE denotes 25-mm PE and PE–Al adds 0.5-mm downstream Al. Percentages refer to total silicon deposited energy, not particle counts.

| Quantity | None | PE | PE–Al |
|---|---|---|---|
| Total (keV/primary) | 0.905383 | 1.30902 | 1.22497 |
| Depositing species (% of total) | | | |
| Secondary $e^-$ | 99.2043 | 98.3998 | 97.9702 |
| $e^+$ | 0.7911 | 1.5976 | 2.0266 |
| All $\gamma$ tracks | 0.00462 | 0.00263 | 0.00322 |
| All other species | 0 | 0 | 0 |
| Immediate birth volume of secondary tracks (%) | | | |
| Al | 0 | 0 | 9.8151 |
| PE | 0 | 30.3404 | 19.1777 |
| Silicon | 96.7949 | 68.7308 | 70.3383 |
| World (air) | 3.2013 | 0.9270 | 0.6665 |

## 4.2 Proton critical-thickness behaviour

The proton-thickness scans exhibited a pronounced non-monotonic detector response. Increasing the PE thickness initially increased the silicon energy deposition before producing effective primary-proton suppression.

In the exploratory three-seed thickness scan, using $5 \times 10^4$ primaries per seed, the 30 MeV response reductions at 6 mm, 7 mm, and 8 mm PE were $-73.60 \pm 0.52\%$, $-129.02 \pm 0.17\%$, and $-258.67 \pm 1.04\%$, respectively. At 9 mm, the response changed abruptly to $99.9981 \pm 0.0017\%$.

Transport-stage scoring explains this transition. In the unshielded configuration, 99.822% of the primary protons entered the silicon with a mean kinetic energy of 29.580 MeV. With 8 mm PE, 95.843% still reached the sensor, but their mean entry energy decreased to $6.667 \pm 0.006$ MeV. The mean silicon energy deposition per generated primary, including zero-deposition histories, increased from approximately 1.779 MeV in the unshielded case to 6.385 MeV. Thus, the PE layer slowed the protons without stopping them, shifting the transmitted population into a regime of substantially greater energy deposition in silicon.

At 9 mm, the forward-exit fraction fell to approximately 0.010% and the primary sensor-entry fraction to $0.0033 \pm 0.0038\%$, marking the transition to effective range-out.

The same mechanism was observed for 50 MeV protons in the step-26 pencil-beam diagnostic. At 20 mm PE, 92.616% of the primary protons still entered silicon with a mean entry energy of $13.307 \pm 0.008$ MeV. Mean silicon deposition was 3.40977 MeV per generated primary, compared with 1.17382 MeV in the matched unshielded sample. The response therefore increased by about a factor of 2.90. This is distinct from the $-89.76 \pm 0.73\%$ response of the 20-mm PE candidate in the final square-source geometry (Table 8); that value must not be assigned to the pencil-beam transport curve. At 25 mm, the forward-exit

fraction decreased to $0.0027 \pm 0.0014\%$, no primary-proton sensor entry was observed, and the residual event-averaged silicon deposition was approximately $8.2 \times 10^{-6}$ MeV/event. Zero observed primary entries and this nonzero all-particle deposition are separate results. The documented sample contains $3 \times 10^5$ primary histories for this condition, giving the one-sided 95% entry-probability upper bound $9.98572 \times 10^{-6}$ (0.000998572%). The residual deposition is retained as a finite-statistics point estimate rather than replaced by zero.

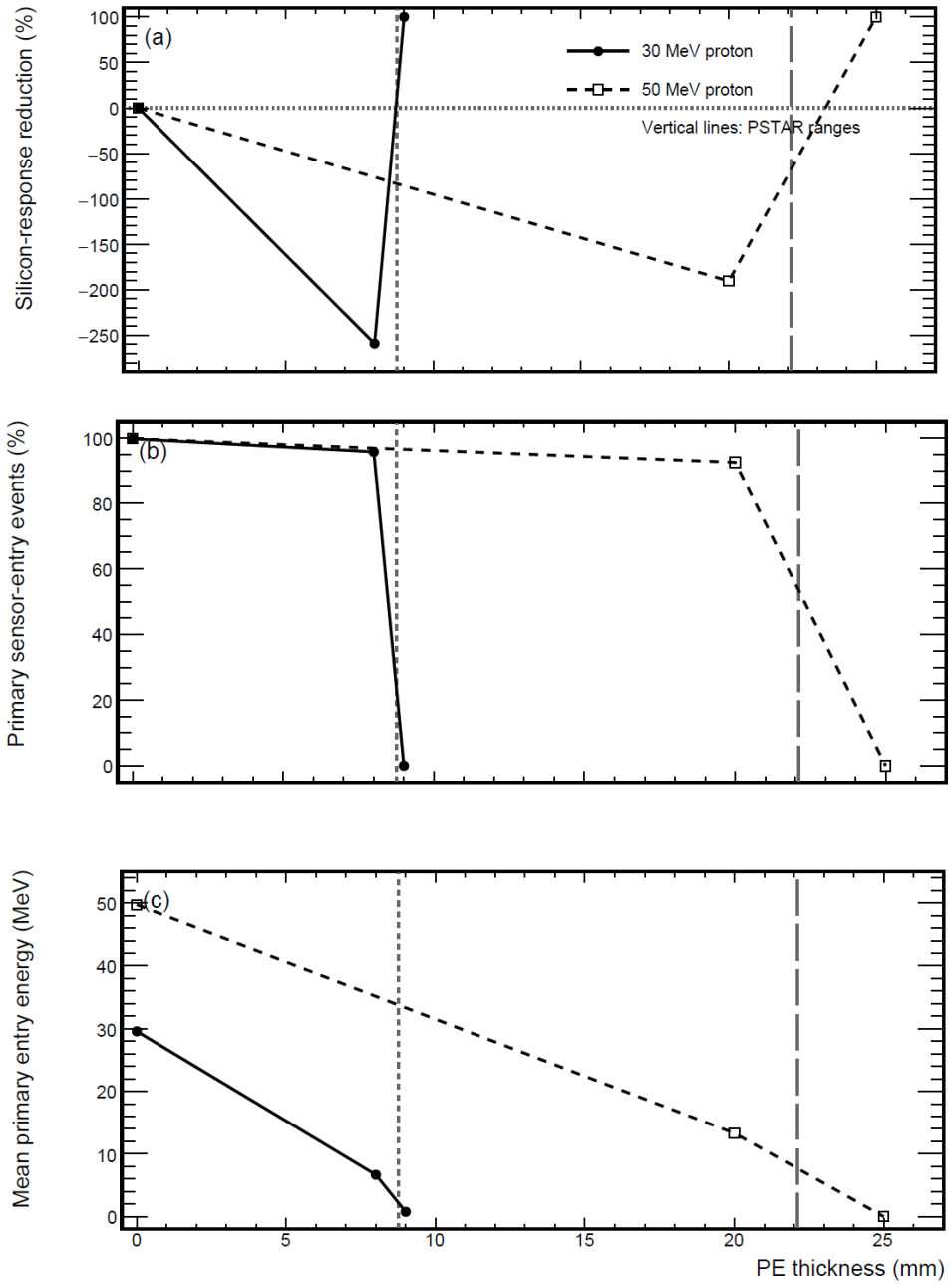


Figure 3. Proton response across the PE critical-thickness regions for 30 MeV and 50 MeV protons: (a) silicon-response reduction, (b) primary-proton sensor-entry fraction, and (c) mean kinetic energy at first sensor entry. The vertical reference lines denote the corresponding PSTAR projected ranges in polyethylene. Error bars represent two-sided 95% confidence intervals from three independent seeds of $10^5$ primaries in the step-26 pencil-beam campaign ($W = 100$ mm, $g = 20$ mm). All panels use that campaign, not the final square-source candidate comparison. Entry energies are conditional on an observed entry; deposition is averaged over all generated primaries.

The critical transition therefore occurred between 8–9 mm PE for 30 MeV protons and between 20–25 mm PE for 50 MeV protons, consistent with the independent PSTAR comparison in Section 3.4. The result demonstrates that charged-particle shielding cannot be ranked by nominal thickness or energy loss alone: primary survival, residual entry energy, and detector energy deposition must be evaluated jointly.

## 4.3 Finite lateral containment at oblique incidence

Table 6.
One-sided 95% upper bounds for diagnostic conditions reporting zero original-primary proton entries, from Eq. 5. All use a pencil source and $g = 20$ mm. Each energy, angle, and side length listed is a separate condition; $N$ is not pooled across them.

| Condition | Shield side / angle | $N$ per condition | $p_{\mathrm{entry},U}$ | $100p_{\mathrm{entry},U}$ (%) |
|---|---|---|---|---|
| Step 26: 50 MeV; 25-mm PE | 100 mm / 0° | 300000 | $9.98572 \times 10^{-6}$ | 0.000998572 |
| Step 27: 30 MeV; 9-mm PE | 100 mm / 30°, 45° | 90000 | $3.32854 \times 10^{-5}$ | 0.00332854 |
| Step 27: 50 MeV; 25-mm PE | 100 mm / 0°, 30°, 45° | 90000 | $3.32854 \times 10^{-5}$ | 0.00332854 |
| Step 27A: 30 MeV / 9-mm PE; 50 MeV / 25-mm PE | 200, 300 mm / 60° | 300000 | $9.98572 \times 10^{-6}$ | 0.000998572 |

The oblique-incidence calculations showed that sufficient nominal thickness does not guarantee particle containment when the lateral shield dimensions are limited. Figure 4(a) compares incidence angles of $0^\circ$, $30^\circ$, $45^\circ$, and $60^\circ$ for the stopping-thickness pairs 30 MeV/9 mm PE and 50 MeV/25 mm PE. Figure 4(b) then holds the incidence angle at $60^\circ$ and increases the square shield side length from 100 mm to 200 mm and 300 mm.

For 30 MeV protons incident on 9 mm PE, a 100 mm square layer produced a primary sensor-entry fraction of $0.0060 \pm 0.0066\%$. No primary sensor entry was observed after the lateral dimension was increased to 200 mm or 300 mm within the corresponding simulated samples.

The effect was much stronger for 50 MeV protons incident on 25 mm PE. With a 100 mm square shield, $90.653 \pm 0.295\%$ of the primaries entered the silicon with a mean entry energy of $21.413 \pm 0.007$ MeV. Increasing the lateral dimension to 200 mm eliminated the observed primary sensor-entry population and reduced the residual event-averaged silicon deposition to approximately $6.2 \times 10^{-6}$ MeV/event. A further increase to 300 mm produced no resolved additional benefit.

The recorded direct-bypass fraction was zero: the sensor-reaching original primaries had a PE-entry checkpoint. This establishes PE intersection, but does

not establish traversal of its full normal thickness. With the aiming rule in Eq. 1, the nominal $60^\circ$ ray for 25-mm PE and a 20-mm axial gap crosses the PE front and rear planes at $x = -78.38$ and $-35.07$ mm, respectively. For a 100-mm square shield, the front-plane intercept lies outside the edge $x = -50$ mm, whereas the rear-plane intercept lies inside. The unscattered ray therefore enters through the side and crosses only about 17.24 mm of PE, rather than the 50-mm infinite-slab path. A 200-mm side contains both intercepts. These geometric calculations explain an edge-clipped material path without requiring an unverified claim of lateral exit. Scattering and energy-loss fluctuations remain part of the simulated trajectories.

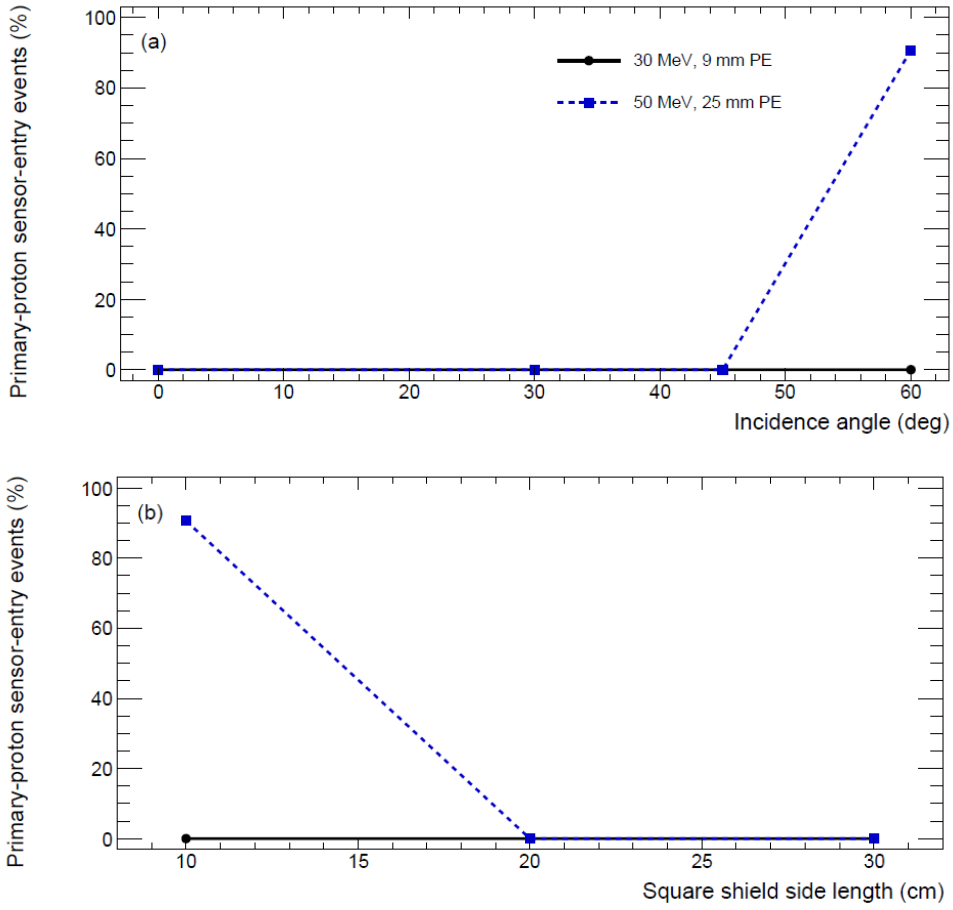


Figure 4. Effect of incidence angle and finite lateral dimensions on primary proton transport: (a) angle scan for 30 MeV protons with 9 mm PE and 50 MeV protons with 25 mm PE using a 100-mm square shield; and (b) side-length scan at $60^\circ$ . The 100-mm shield did not laterally contain the oblique 50 MeV trajectories, whereas a 200-mm side length suppressed the observed primary sensor entry. Both panels use a pencil beam and $g = 20$ mm; panel (a) uses $3 \times 30000$ primaries per condition and panel (b) uses $3 \times 100000$ .

The $200\ \text{mm} \times 200\ \text{mm}$ square geometry was therefore adopted for the final benchmark comparison. This dimension is specific to the present source position, incidence geometry, sensor area, and shield-to-sensor spacing; the general result is that lateral coverage must be verified independently of one-dimensional stopping thickness.

The zero-entry conditions from the normal, angle, and side-length diagnostics are collected in Table 6. A zero-entry point and a vanishing empirical run-to-run

error bar are not evidence of zero transmission probability. The numerical limits below are one-sided bounds on original-primary entry only.

## 4.4 Final multi-field performance

The two selected configurations were evaluated using five independent seed-index-matched simulations under the benchmark photon, electron, 30 MeV proton, and 50 MeV proton fields. The results are summarised in Table 7.

Table 7.
Five-seed final comparison of the selected shielding configurations. Uncertainties are two-sided 95% sampling confidence-interval half-widths conditional on the reference model. Proton values above 99.999% are finite-run energy-response estimates; they are not confidence bounds on primary-proton entry. See Eq. 5.

| Quantity | 25 mm PE | 25 mm PE + 0.5 mm Al |
|---|---|---|
| Photon (%) | $16.547 \pm 3.310$ | $19.630 \pm 3.159$ |
| Electron (%) | $99.020 \pm 0.031$ | $99.161 \pm 0.084$ |
| 30 MeV proton (%) | $> 99.999$ | $> 99.999$ |
| 50 MeV proton (%) | $> 99.999$ | $> 99.999$ |
| Worst field (%) | $16.547 \pm 3.310$ | $19.630 \pm 3.159$ |

The photon field determined the worst-field response for both configurations. Adding 0.5 mm of downstream Al increased the photon-response reduction from $16.547 \pm 3.310\%$ to $19.630 \pm 3.159\%$. The five seed-index-matched differences yielded

$$\Delta P_\gamma = 3.083 \pm 0.558 \text{ percentage points}, \tag{18}$$

with a positive difference for all five seed pairs. The interval covers Monte Carlo sampling variability only, with limits of 2.525 and 3.641 percentage points. The exact improvement remains physics-model dependent; the single-seed Shielding_EMZ test in Section 3.3 is not included in this interval. The aluminium layer produced only a small additional electron improvement (approximately 0.141 percentage points), while no additional proton benefit was resolved because both configurations already suppressed the proton response below the practical statistical resolution of the campaign. The principal benefit of the downstream Al layer was therefore an improvement of the photon-limited response.

## 4.5 Mass–performance trade-off

The equal-statistics candidate comparison is summarised in Table 8. The worst-field metric is retained because averaging over particle species would conceal the strongly adverse response produced by incomplete proton stopping in some intermediate-thickness configurations.

The 15 mm and 20 mm PE configurations illustrate the importance of the worst-field criterion: although both improved the photon and electron responses relative to thinner PE, their 50 MeV proton response became strongly negative

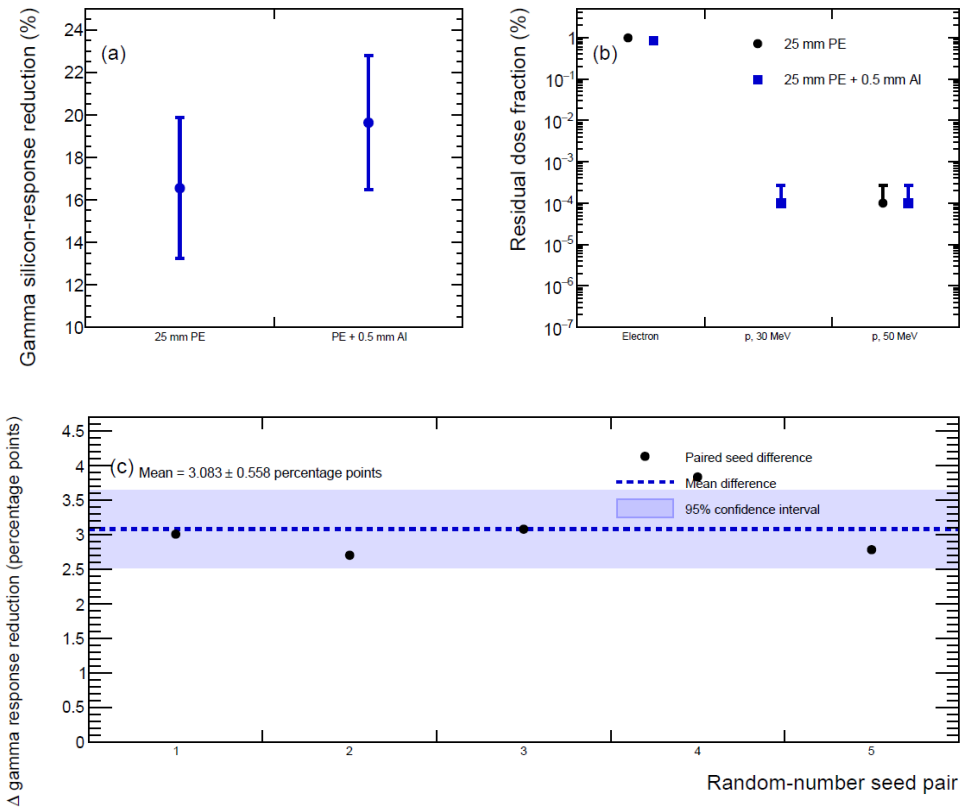


Figure 5. Final five-seed comparison of 25 mm PE and 25 mm PE + 0.5 mm Al: (a) photon-response reduction, (b) residual electron and proton response fractions on a logarithmic scale, and (c) seed-index-matched photon-response improvement produced by the aluminium-backed configuration. The shaded band in panel (c) represents the two-sided 95% sampling confidence interval around the mean paired difference at fixed reference physics list; it excludes physics-model uncertainty. Panel (b) shows residual energy-response ratios, not primary-entry probabilities.

Table 8.
Active shield mass and mean silicon-response reduction for the investigated 200 mm × 200 mm configurations. Photon values correspond to the equal-statistics three-seed comparison. Negative values indicate an increase in silicon response relative to the unshielded reference.

| Configuration | Mass (g) | $P_\gamma$ (%) | $P_e$ (%) | $P_{p30}$ (%) | $P_{p50}$ (%) | $P_{\text{worst}}$ (%) |
|---|---|---|---|---|---|---|
| 9 mm PE | 338.40 | 6.824 | 94.470 | 99.998 | −4.804 | −4.804 |
| 15 mm PE | 564.00 | 9.479 | 97.158 | > 99.999 | −20.970 | −20.970 |
| 20 mm PE | 752.00 | 13.529 | 98.326 | > 99.999 | −89.758 | −89.758 |
| 25 mm PE | 940.00 | 15.821 | 99.016 | > 99.999 | > 99.999 | 15.821 |
| 25 mm PE + 0.5 mm Al | 993.98 | 18.752 | 99.133 | > 99.999 | > 99.999 | 18.752 |
| 25 mm PE + 1.0 mm Al | 1047.96 | 23.104 | 99.301 | > 99.999 | > 99.999 | 23.104 |

because the shield slowed, but did not stop, most of the incident protons. The 9 mm configuration was lighter but likewise failed to provide positive response reduction across all four fields.

Within the investigated discrete candidate set, 25 mm PE was therefore the lowest-mass configuration with positive mean response reduction in every benchmark field. Its active shield mass was 940.00 g. Adding 0.5 mm Al increased the

mass to 993.98 g, a penalty of 53.98 g (5.74%), while improving the photon-limited response. The 1.0 mm Al configuration achieved the highest mean photon and worst-field response reduction in the candidate scan (23.104%), but it also had the largest active shield mass (1047.96 g) and was not subjected to the same five-seed final validation as the two selected configurations.

The mass comparison therefore identifies a trade-off rather than a universal optimum: 25 mm PE provides the lower-mass balanced configuration, whereas the 25 mm PE + 0.5 mm Al design provides improved photon-limited performance at a moderate additional mass.

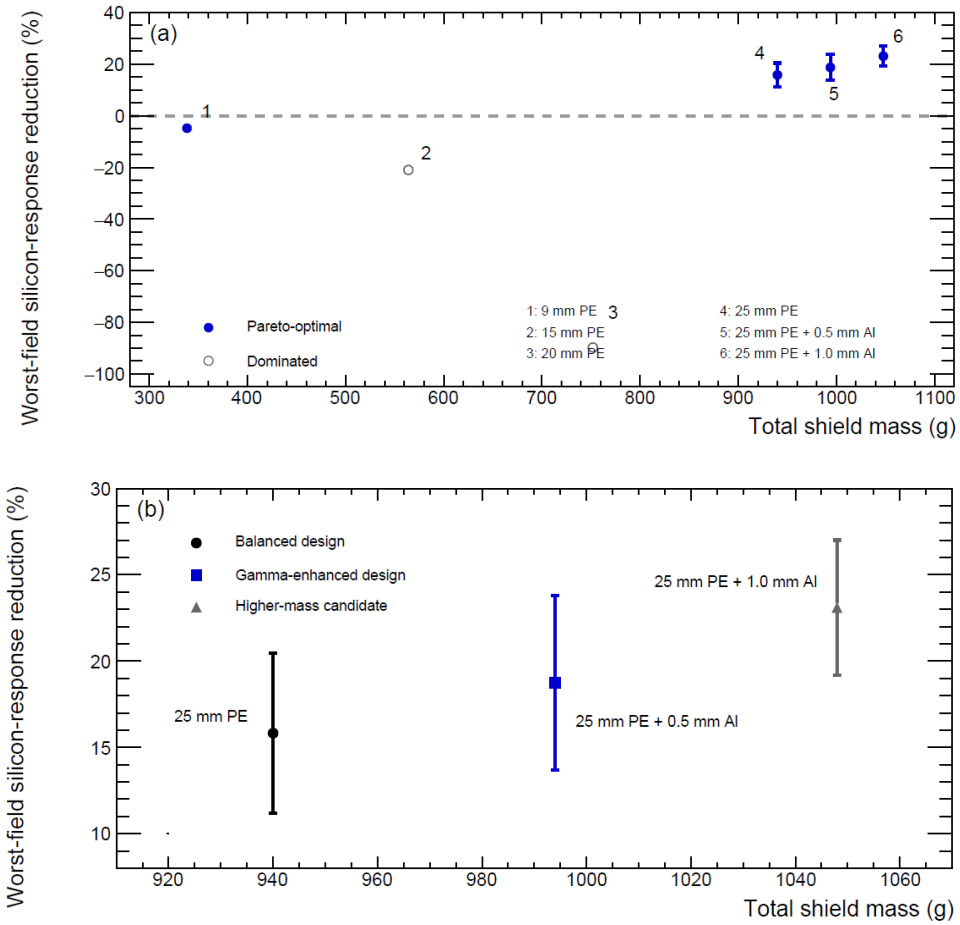


Figure 6. Active mass versus worst-field silicon-response reduction for the discrete candidate set. (a) All six configurations; filled markers are non-dominated when mean response and active mass alone are used, whereas open markers are dominated. A Pareto label does not imply acceptability: the light 9 mm PE candidate remains infeasible under the additional requirement $P_{\mathrm{worst}} > 0$. (b) Expanded comparison of the three candidates with positive mean response reduction in every benchmark field. Their worst field is the photon field, so the vertical intervals are the photon-response confidence intervals from the candidate campaign. Pareto classification is based on central estimates.

Figure 6(a) makes the screening logic explicit. The 15 mm and 20 mm PE candidates are dominated because they add mass while retaining a worse limiting response than another tested design. The 9 mm point is mathematically non-dominated only because it is the lightest candidate; its negative 50 MeV proton response excludes it from the feasible set. Panel (b) therefore isolates the three designs that satisfy the positive-worst-field requirement and shows the incremental mass paid for the two Al-backed photon improvements. The plot and

Table 8 convey complementary information: the table retains the field-by-field mechanism, whereas the plot exposes the mass trade-off used for screening.

### 4.6 Physical implications

The calculations lead to three distinct screening rules. First, a charged-particle layer must be tested on both sides of the expected range-out thickness; testing only a sub-range point can select the most harmful part of the response curve. Second, a photon shield must be evaluated with its actual detector spacing because charged-secondary acceptance can reverse an attenuation-based ranking. Third, adequate normal thickness must be accompanied by an explicit lateral-containment test at the relevant angles.

Previous work has addressed multilayer materials, secondary production, and mass-dependent performance [5, 6]. The advance of the present framework is to connect these effects to a common detector-level diagnostic record: primary survival, residual energy, secondary origin, boundary-crossing history, and sensitive-volume energy deposition. Coupling those observables to a positive-worst-field feasibility condition prevents a favourable photon or electron result from hiding a damaging proton regime. The method is therefore suited to early numerical screening; platform-specific spectra, packaging, and experimental qualification remain necessary before a shield can be prescribed for service.

## 5. Limitations and applicability

The present study was designed as a controlled, mechanism-resolved benchmark rather than as a mission-specific shielding qualification. The quantitative results should therefore be interpreted within the defined irradiation fields, material set, geometry, and silicon detector model.

### 5.1 Benchmark and model scope

The photon and electron calculations used a common discrete particle-number distribution spanning 0.1–10 MeV, while the proton calculations used monoenergetic 30 MeV and 50 MeV primaries. These fields were selected to isolate energy-dependent transport mechanisms under controlled conditions and do not represent a measured atmospheric, orbital, accelerator, reactor, or platform-specific radiation environment. Real fields may contain continuous spectra, broad angular distributions, mixed particle populations, temporal variations, and contributions from surrounding structures. The reported response reductions should therefore not be interpreted directly as mission-specific dose-reduction factors. In particular, the sharp proton critical-thickness transitions obtained here would be broadened under a continuous proton spectrum as different energy components range out at different depths.

The protected component was represented by a homogeneous planar silicon sensitive volume rather than a complete packaged device. Sensor housings,

passivation and readout structures, printed-circuit boards, connectors, mechanical supports, adhesives, and surrounding platform materials were not included. Such materials could modify both the incident field and the secondary-particle environment. Likewise, the final $200\ \text{mm} \times 200\ \text{mm}$ shield area and 100 mm shield-to-sensor gap are specific to the benchmark geometry used to suppress the lateral-containment and short-gap secondary-transport effects identified in this study; they should not be interpreted as universal packaging dimensions.

The material space was restricted to PE and downstream Al, and the thickness scan was discrete. Other candidate materials, graded-$Z$ structures, borated or high-hydrogen-content composites, alternative layer orders, and continuously varied geometries were outside the present scope. Consequently, the identified 25 mm PE and PE–Al configurations represent favourable candidates within the investigated design set rather than global shielding optima. Reported masses include only the active PE and Al volumes and exclude structural integration, bonding, manufacturing tolerances, and packaging hardware.

## 5.2 Numerical, physics-model, and detector-response limitations

All particle transport was calculated with Geant4. Numerical and physical consistency were examined through repeated-seed simulations, production-cut refinement, an alternative electromagnetic transport configuration, transport-stage scoring, and comparisons with NIST PSTAR, ESTAR, and XCOM reference data. These checks probe different aspects of the calculation but do not constitute experimental validation or an independent second-code benchmark.

The electromagnetic-model comparison showed that this limitation is not uniform across all configurations. In the photon sensitivity test, the PE-only response changed from 15.322% with Shielding to 9.071% with Shielding_EMZ, whereas the PE–Al result changed only from 18.331% to 18.445%. Because this comparison used one random seed per physics configuration, it should be interpreted as evidence of model sensitivity rather than as a quantitative transport-model uncertainty estimate.

In particular, the aluminium-backed minus PE-only photon contrast was 3.009 percentage points in the single-seed reference-list test and 9.374 percentage points in the corresponding `Shielding_EMZ` test. The five-seed value of $3.083 \pm 0.558$ percentage points therefore characterises the reference-list sampling distribution only; it is not a model-independent prediction with a total uncertainty of 0.558 percentage points.

The reported confidence intervals describe Monte Carlo sampling variability across repeated runs and do not include uncertainties in interaction models, cross sections, material composition, density, source specification, or manufacturing tolerances. Rare residual responses near complete proton suppression are additionally limited by finite event statistics. The zero-count limits in Table 6 use the diagnostic event counts documented in the run scripts and analysis normalisations. They constrain original-primary entry, not the nonzero energy deposited by all transported particles. The final $P > 99.999\%$ values remain energy-response point estimates, not binomial limits or total-uncertainty guarantees. The available

quantitative species/origin partition belongs to the 20-mm-gap pencil-beam diagnostic; extending it to the final square-source 100-mm-gap geometry would require extracting the corresponding tallies.

Finally, the principal detector-response quantity was the energy deposited in the silicon sensitive volume. This observable is directly related to ionising energy absorption but does not by itself predict complete device performance or lifetime. Displacement damage, non-ionising energy loss, single-event effects, charge-collection changes, dark-current increase, threshold shifts, and permanent functional degradation were not modelled. Translation of the present transport results into component reliability would require device-specific response data and experimental qualification.

### 5.3 Applicability

Within these boundaries, the framework is intended as an early-stage numerical screening approach for identifying transport mechanisms that can be missed by attenuation or one-dimensional range estimates alone. In particular, it can identify harmful partial proton stopping, shield-generated secondary-particle contributions, insufficient lateral containment, and configurations that fail under one field despite performing favourably under others.

Application to a specific sensor or platform would require replacing the benchmark fields and geometry with the relevant particle spectra, angular and spatial distributions, packaged-device geometry, surrounding materials, and mission fluence or dose normalisation. Component-specific damage or failure criteria would then be required to connect the simulated energy deposition to operational performance.

The present results should therefore be regarded as a mechanism-resolved physical benchmark and candidate-screening framework, rather than as a final shield specification for a particular aerospace, defence, or electronic platform.

## 6. Conclusion

Detector-level scoring revealed three regimes that a thickness-only assessment would miss. Partial proton slowing increased silicon energy deposition immediately below range-out, with transitions at 8–9 mm PE for 30 MeV and 20–25 mm PE for 50 MeV; both intervals contain the corresponding PSTAR projected range. The photon gap dependence was consistent with geometric acceptance of secondary particles and scattered photons, while oblique protons exposed a separate edge-coverage failure mode. The existing short-gap tally quantified a 28.99–30.34% contribution from shield-born secondary tracks to total silicon deposition; it is not transferred numerically to the final geometry.

For the final 100 mm gap, adding 0.5 mm downstream Al to 25 mm PE improved photon-response reduction by $3.083 \pm 0.558$ percentage points under Shielding, where the 95% interval represents sampling uncertainty only. The improvement magnitude remains model-dependent. The 1.01-percentage-point

XCOM estimate measures additional uncollided primary-photon number removal; its different weighting and normalisation preclude interpreting its difference from the detector-response change as a secondary-energy contribution. Within the tested design set, 25 mm PE was the least massive candidate with positive mean response reduction in every field; the Al-backed version added 53.98 g (5.74%) and improved the photon-limited response.

The practical conclusion is that range, attenuation, and areal mass are necessary but insufficient screening variables. Primary survival, residual energy, secondary transport, detector spacing, and lateral coverage must be evaluated together. The numerical values remain conditional on the benchmark spectra, geometry, PE/Al material set, and Geant4 models, and should not be interpreted as a flight- or platform-qualified shield prescription.

## Acknowledgement

The author acknowledges the Geant4 and ROOT collaborations for developing and maintaining the simulation and data-analysis frameworks used in this work.

## Data and code availability

The LaTeX source, bibliography, and publication-quality figures are included in the manuscript package. Simulation inputs, analysis macros, and processed event data are available from the corresponding author on reasonable request.

## Declaration of generative AI and AI-assisted technologies

During the preparation of this manuscript, the author used ChatGPT (OpenAI) for assistance with manuscript organisation, English-language refinement, LaTeX preparation, and code troubleshooting. All AI-assisted material was critically reviewed and verified by the author. The author takes full responsibility for the simulation methodology, data analysis, physical interpretation, and final content of the manuscript.

## References

[1] J.R. Srour, J.M. McGarrity, Proceedings of the IEEE **76** (1988) 1443–1469.[*Web link*]
[2] G.C. Messenger, M.S. Ash, The Effects of Radiation on Electronic Systems, 2nd ed. (Van Nostrand Reinhold, New York, 1992) 951 p. [*Web link*]
[3] R.H. Maurer, M.E. Fraeman, M.N. Martin, D.R. Roth, Johns Hopkins APL Technical Digest **28** (2008) 17–29. [*Web link*]

[4] S. Bourdarie, M. Xapsos, IEEE Transactions on Nuclear Science **55** (2008) 1810–1832. [*Web link*]
[5] H. Daneshvar et al., Scientific Reports **11** (2021) 20657. [*CrossRef*]
[6] A. Gohel, R. Makwana, Radiation Physics and Chemistry **197** (2022) 110131. [*CrossRef*]
[7] A. Fetzer, M. Anger, P. Oleynik, J. Praks, Advances in Space Research **73** (2024) 831–845. [*CrossRef*]
[8] J. Su et al., Advances in Space Research **73** (2024) 2652–2662. [*CrossRef*]
[9] F. Cordella et al., The European Physical Journal Plus **139** (2024) 150. [*CrossRef*]
[10] M.J. Berger et al., ESTAR, PSTAR, and ASTAR: Computer Programs for Calculating Stopping-Power and Range Tables for Electrons, Protons, and Helium Ions, Version 1.2.3, National Institute of Standards and Technology, Gaithersburg, MD, 2005. [*Web link*]
[11] M.J. Berger et al., PSTAR: Stopping-Power and Range Tables for Protons, National Institute of Standards and Technology, Gaithersburg, MD, 2005. [*Web link*]
[12] International Commission on Radiation Units and Measurements, Stopping Powers and Ranges for Protons and Alpha Particles, ICRU Report 49, Bethesda, MD, 1993. [*CrossRef*]
[13] M.J. Berger et al., ESTAR: Stopping-Power and Range Tables for Electrons, National Institute of Standards and Technology, Gaithersburg, MD, 2005. [*Web link*]
[14] International Commission on Radiation Units and Measurements, Stopping Powers for Electrons and Positrons, ICRU Report 37, Bethesda, MD, 1984. [*Web link*]
[15] M.J. Berger et al., XCOM: Photon Cross Section Database, Version 1.5, National Institute of Standards and Technology, Gaithersburg, MD, 2010. [*Web link*]
[16] S. Agostinelli et al., Nuclear Instruments and Methods in Physics Research Section A **506** (2003) 250–303. [*CrossRef*]
[17] J. Allison et al., IEEE Transactions on Nuclear Science **53** (2006) 270–278. [*CrossRef*]
[18] J. Allison et al., Nuclear Instruments and Methods in Physics Research Section A **835** (2016) 186–225. [*CrossRef*]
[19] R. Brun, F. Rademakers, Nuclear Instruments and Methods in Physics Research Section A **389** (1997) 81–86. [*CrossRef*]
[20] Geant4 Collaboration, Guide for Physics Lists, Geant4 Version 11.2, Geant4 Documentation, 2023. [*Web link*]
[21] Geant4 Collaboration, Shielding Reference Physics List, Geant4 Version 11.2, Geant4 Physics List Guide, 2023. [*Web link*]
[22] NIST/SEMATECH, e-Handbook of Statistical Methods, Section 7.2.4.1: Confidence Intervals for a Binomial Proportion, National Institute of Standards and Technology. [*Web link*]